"Coiling of elastic rods on rigid substrates"
Supplementary Information

Jawed et al.

S1 Static coiling: interplay of natural curvature and twist

In the main manuscript, we studied the scenario of static coiling when an elastic rod is deployed onto a rigid substrate (when the belt is static, $v_b = 0$), giving particular emphasis to the interplay between natural curvature and twist. This was motivated by the finding that, for nearly straight rods, the coiling is smooth (see Movie S1) and the rod prescribes a circle on the substrate with a coiling radius that is set by the gravito-bending length, $\bar{R}_C \sim 2$, *i.e.* $R_C \sim 2L_{gb}$ (Fig. 2*C* in main manuscript). By contrast, for a sufficiently curved rod, the coiling radius is set but its natural radius $\bar{R}_n = 1/\bar{\kappa}_n$ and the coiling direction exhibits periodic reversals (see Movie S2). Recall from the manuscript that barred quantities represent normalization of length by the gravito-bending length, L_{gb}, and time by L_{gb}/v. In what follows, we extend the analysis of the data obtained from the DER simulations that was presented in Fig. 2*D* and Fig. 2*E* of the main manuscript.

In Fig. S1*A*, we plot simulated results for a representative time-series of the total twist, $\Phi(\bar{t}) = \int_0^{s_c} \theta'(s,\bar{t})ds$, accumulated on the suspended heel (between the injector, at $s = 0$, and the point of contact with the substrate, $s = s_c$) for a rod with $\bar{\kappa}_n = 0.69$, $L_{gb} = 3.3$ cm, deployed from $\bar{H} = 15$. The maxima and minima of $\Phi(\bar{t})$ are associated with events of inversion of the coiling direction, which are marked in the plot by the vertical solid lines. The reversal events were identified independently and automatically by examining the signed turning angle in the conveyor belt's plane between successive edges in spatial discretization of the simulations. The corresponding rate of accumulation of total twist, $\mathrm{d}\Phi/\mathrm{d}\bar{t}$, is plotted in Fig. S1*B*. Prior to each reversal event, $\mathrm{d}\Phi/\mathrm{d}\bar{t}$ is approximately constant, which is consistent with the radial symmetry of the geometry of deposition onto the belt. Immediately after each reversal, however, there is an abrupt step-change in stored twist, which is consistent with and provides further evidence for the torsional buckling instability mentioned in the main text.

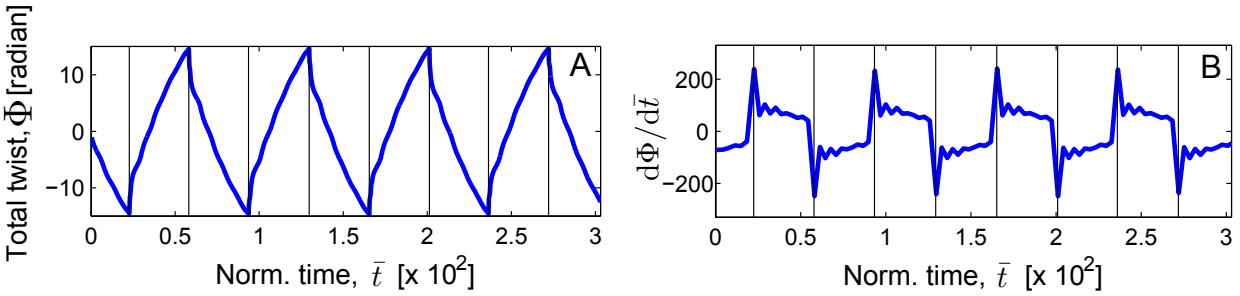

Figure S1: Static coiling. Time series of (A) the total twist, $\Phi(\bar{t})$, and (B) its time derivative, $\mathrm{d}\Phi/\mathrm{d}\bar{t}$, accumulated on the suspended heel, between the injector and the contact point with the substrate. The data was obtained from the DER simulations for a naturally curved rod with $L_{gb} = 3.3$cm and $\bar{\kappa}_n = 0.69$, that was deployed from a height of $\bar{H} = 15$. The vertical solid lines correspond to events of reversal of the coiling direction.

S1 STATIC COILING: INTERPLAY OF NATURAL CURVATURE AND TWIST

We now further address the relation between storage of twist and the inversion of the coiling direction by quantifying the average twist at inversion, $\theta'_c = \Phi_c/s_c$, where Φ_c corresponds to the maxima in the time series of Fig. S1. Under the approximation that $s_c \approx H$, the dimensionless average twist at inversion becomes,

$$\bar{\theta}'_c = \frac{\Phi_c}{\bar{H}}. \tag{S1}$$

In Fig. S2*A*, we plot $\Phi_c/(2\pi)$ as a function of the number of coils between each inversion, $N = \bar{L}_{inv}/(2\pi\bar{R}_C)$, where $\bar{L}_{inv}$ is the dimensionless length of the segment of the rod consumed between each reversal. We find that $\Phi_c/(2\pi)$ depends linearly on N, with approximately the same slope of ~ 0.5 for different values of $\bar{\kappa}_n$. Recalling that the total twist oscillates between $-\Phi_c$ and Φ_c (Fig. S1*A*), we conclude that each coil accumulates an amount of 2π of total twist, which was a result needed in the main manuscript. Moreover, the dependence of the total twist at inversion on the deployment height is plotted in Fig. S2*B*, where we find that $\Phi_c \sim \bar{H}$. This points to the existence of a critical dimensionless twist, $\bar{\theta}'_c$ (defined in Eq. S1), that is independent of $\bar{H}$ and, therefore, further corroborates the scenario of torsional buckling.

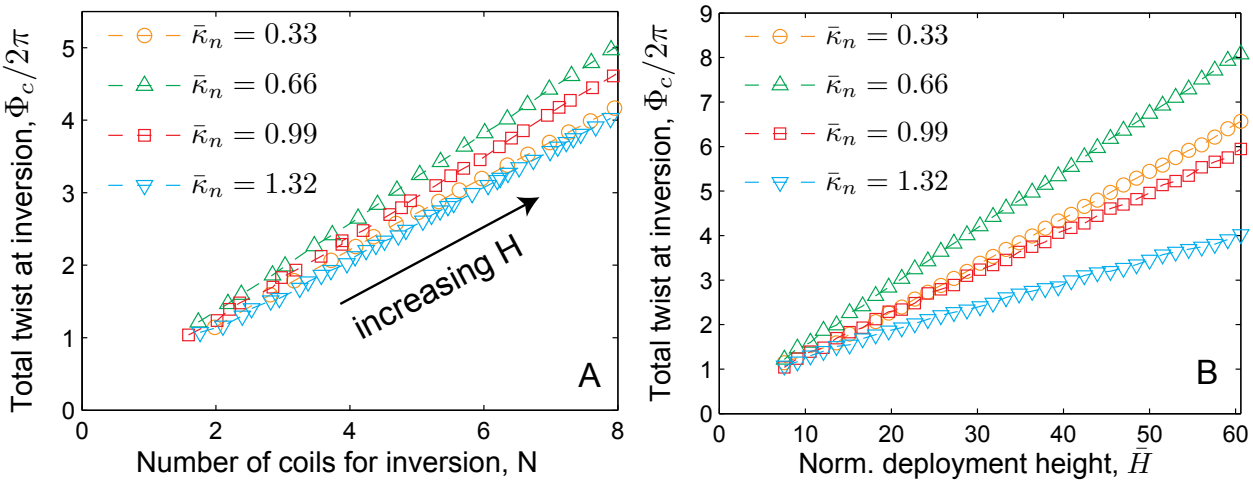

Figure S2: Static coiling. (A) Total twist at inversion, $\Phi_c/(2\pi)$, as a function of the number of coils between each inversion, N ($L_{gb} = 3.3$cm and $\bar{H} = 15$), for rods with different values of the natural curvature $\bar{\kappa}_n$ (provided in the legend). (B) Total twist at inversion, $\Phi_c/(2\pi)$, as a function of normalized deployment height, $\bar{H}$. The data was obtained from the DER simulations.

Thus far, we have focused on the accumulation of twist on the suspended heel of the rod during coiling. In the manuscript, however, we claimed that natural curvature of the rod determines whether the twist in the *suspended heel* can reach the level necessary for torsional buckling, or is held constant by storing additional twist in the loops of rod deposited on the substrate. In Fig. S3 to distinguish between the two regimes, we plot the normalized average twist $\langle\bar{\theta}'\rangle$ in *the deposited loops* (in contrast to the suspended heel, addressed above) as a function of the dimensionless natural curvature, $\bar{\kappa}_n$. This twist is averaged over $60L_{gb}$ of deposited rod, beyond the point of contact with the substrate. Two markedly different regimes emerge. For rods with low natural curvature, $\bar{\kappa}_n < 0.3$, all of the average twist accumulates in the deposited loops. On the other hand, for values of the natural curvature above, $\bar{\kappa}_n > 0.3$, no twist accumulates in the deposited loops requiring that, instead, it is stored in the suspended heel. Above a critical value, this build up of twist then leads to torsional buckling and subsequently to inversion of the coiling direction.

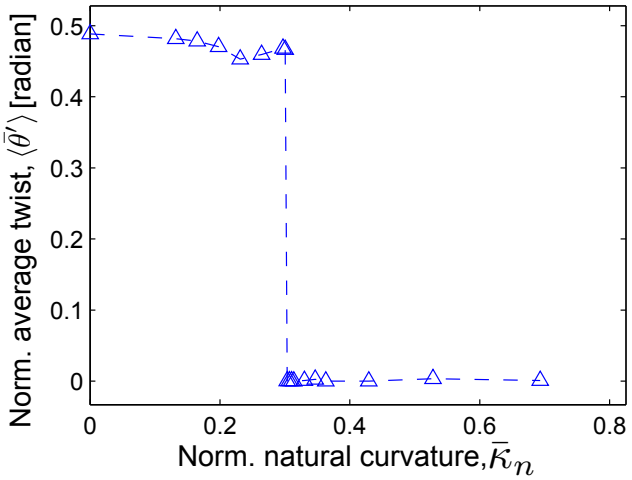

Figure S3: Normalized average twist, $\langle\bar{\theta}'\rangle = \langle\theta'\rangle L_{gb}$, in the deposited loops (averaged over $60L_{gb}$ of rod beyond the point of contact, s_c, with the substrate) as a function of natural curvature. The data was obtained from the DER simulations for a naturally curved rod with $L_{gb} = 3.3$cm that was deployed from a height of $\bar{H} = 15$.

S2 Derivation of geometric relation between $\bar{\lambda}$, $\bar{A}_0$ and ϵ

In Eq. 5 of the manuscript, we stated that the relation between the dimensionless wavelength, $\bar{\lambda}$, of the sinusoidal meandering patterns and the dimensionless characteristic amplitude, $\bar{A}_0$, (set by the physical properties of the rod) is given by

$$\bar{\lambda} = \bar{A}_0(C_1\epsilon + C_2), \tag{S2}$$

where $\epsilon = (v - v_b)/v$ is the dimensionless speed mismatch between the injector and the belt, $\bar{A} = \bar{A}_0\sqrt{\epsilon}$ is the observed amplitude of the patterns and $C_1 = -2.48$ and $C_2 = 3.20$ are numerical coefficients. In the following, we provide a detailed geometry-based derivation of this result.

We start by assuming that the periodic pattern in the meandering regime can be represented by the curve

$$y = A\sin\left(\frac{2\pi x}{\lambda}\right), \tag{S3}$$

where (x, y) is the Cartesian coordinate system on the plane of the belt, and x points along the direction of motion of the belt. The arc length of this curve for a single period of oscillation is given by

$$l = \int_0^{\lambda} \sqrt{1 + \left(\frac{\mathrm{d}y}{\mathrm{d}x}\right)^2}\,\mathrm{d}x, \tag{S4}$$

which can be expressed in terms of the complete elliptical integral of second kind, $E(k) = \int_0^{\pi/2} \sqrt{1 - k^2\sin^2\theta}\mathrm{d}\theta$, as

$$l = \frac{2\sqrt{\lambda^2 + 4\pi^2A^2}}{\pi} E\left(\frac{2\pi A}{\sqrt{\lambda^2 + 4\pi^2A^2}}\right). \tag{S5}$$

Expressing $E(k)$ by the power series

$$E(k) = \frac{\pi}{2}\sum_{n=0}^{\infty}\left\{\frac{(2n)!}{2^{2n}(n!)^2}\right\}^2 \frac{k^{2n}}{1-2n}, \tag{S6}$$

observing that $k = 2\pi A/\sqrt{\lambda^2 + 4\pi^2 A^2} < 1$, and ignoring terms of $O(k^4)$, we obtain

$$l = \sqrt{\lambda^2 + 4\pi^2 A^2}\left(1 - \frac{1}{4}\frac{4\pi^2 A^2}{\lambda^2 + 4\pi^2 A^2}\right). \tag{S7}$$

Under the above assumption of a sinusoidal pattern, the dimensionless speed mismatch (which is treated as the primary control parameter of the dynamic coiling regime) can be written in the alternative form

$$\epsilon = \frac{l - \lambda}{l}. \tag{S8}$$

Combining Eq. S7 and Eq. S8, l can now be eliminated to arrive at

$$\frac{\lambda}{1-\epsilon} = \sqrt{\lambda^2 + 4\pi^2 A^2}\left(1 - \frac{1}{4}\frac{4\pi^2 A^2}{\lambda^2 + 4\pi^2 A^2}\right), \tag{S9}$$

which, upon rearrangement, yields an expression for the meandering wavelength as a function of ϵ,

$$\lambda = A\frac{3\pi(1-\epsilon)}{\sqrt{-1 - 3\epsilon^2 + 6\epsilon + \sqrt{1 - 3\epsilon^2 + 6\epsilon}}}. \tag{S10}$$

Recalling that we found experimentally (Fig. 4*C* of the main manuscript) that $A = A_0\sqrt{\epsilon}$, where A_0, is a constant set by the physical properties of the rod, Eq. S10 can now be rewritten as

$$\lambda = A_0 f(\epsilon), \tag{S11}$$

where $f(\epsilon)$ is a dimensionless function given by

$$f(\epsilon) = \frac{3\pi(1-\epsilon)\sqrt{\epsilon}}{\sqrt{-1 - 3\epsilon^2 + 6\epsilon + \sqrt{1 - 3\epsilon^2 + 6\epsilon}}}. \tag{S12}$$

Note that, in the limit of $\epsilon \to 0$, we obtain $f(\epsilon) \to \pi$. We now seek to find a simpler version of Eq. S12 for small values of ϵ. In our experiments, we find that the meandering regime is restricted to the range $0 < \epsilon < 0.5$ of the control parameter. Within this limited range, we can linearize $f(\epsilon)$ to get

$$f(\epsilon) = -2.48\epsilon + 3.2, \tag{S13}$$

which upon substitution into Eq. S11 yields a simple relation between λ and ϵ,

$$\lambda \approx A_0(-2.48\epsilon + 3.2). \tag{S14}$$

Dividing both sides of Eq. S14 by L_{gb} for the purpose of nondimensionalization leads to

$$\bar{\lambda} \approx \bar{A}_0(-2.48\epsilon + 3.2). \tag{S15}$$

Comparing this result with Eq. 5 of the main manuscript (identical to Eq. S2, above), we can finally determine the values of the originally stated numerical coefficients $C_1 = -2.48$ and $C_2 = 3.20$. Moreover, the dimensionless onset wavelength, $\bar{\lambda}_0$, can also be readily obtained from Eq. S15 by taking the limit of $\epsilon \to 0$, such that $\bar{\lambda}_0 \approx 3.2\bar{A}_0$.

We proceed by performing a quantitative comparison of the dimensionless ratio $f(\epsilon) = \lambda/A_0$ between: i) the full analytical expression (Eq. S12), ii) its linearized version (Eq. S13) and iii) the numerical results obtained directly from the Discrete Elastic Rods (DER) simulation tool. In the DER numerics, we have measured the amplitude, A, and wavelength, λ, of the sinusoidal patterns in the meandering regime, for different values of ϵ and the constant A_0 was evaluated using the relation $A = A_0\sqrt{\epsilon}$. In these simulations we used a rod with the gravito-bending length $L_{gb} = 3.3$cm, deployed from a height of $\bar{H} = 33$ (same parameters were used for the data reported in Fig. 4 of the main text). In Fig. S4, we plot the results

for the dependence of $f(\epsilon)$ on the dimensionless excess velocity, ϵ, for each of the three cases. Excellent agreement is found between one another, which confirms the validity of the linear approximation in Eq. 5 of the main text, which is an important ingredient throughout the analysis of the meandering regime.

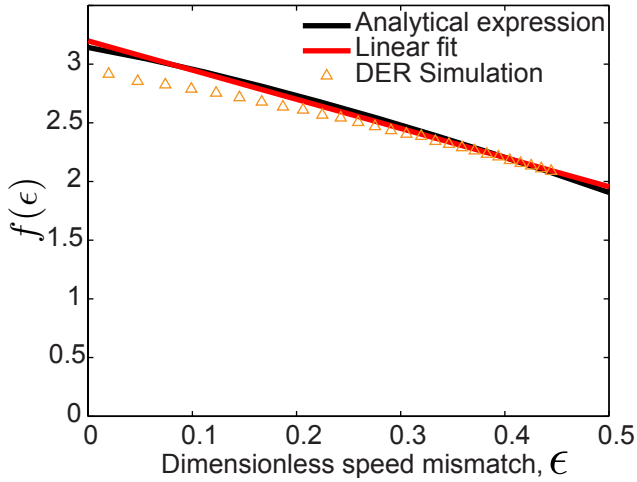

Figure S4: Dependence of the dimensionless ratio $f(\epsilon) = \lambda/A_0$ (defined in Eq. S11) on the dimensionless speed mismatch, ϵ. A comparison is performed for i) the full analytical expression (Eq. S12), ii) its linearized version (Eq. S13) and iii) the numerical results obtained from DER (using a rod with $L_{gb} = 3.3$cm, deployed from $\bar{H} = 33$).

S3 Additional phase diagrams in the $(\bar{\kappa}_n, \epsilon)$ and $(\bar{H},\epsilon)$ parameter spaces

In Fig. 3 of the main text, we presented a phase diagram of the various coiling regimes (I – Meandering; II – Stretched coiling; III – Alternating loops; and IV – Translated coiling) in the (v, v_b) parameter space, for a naturally straight rod ($\bar{\kappa}_n = 0$). Recall that v is the speed of deployment and v_b is the speed of the belt. The linearity of the observed phase boundaries (straight lines that pass through the origin) that separate the various regimes suggested that the primarily control parameter of the patterns was the dimensionless speed mismatch, $\epsilon = (v - v_b)/v$.

Throughout the manuscript, we have also identified other physical parameters that play an important role in the coiling process, namely the natural curvature of the rod, κ_n, and the height of deployment. As such, and for the sake of completeness, we have constructed phase diagrams in the $(\bar{\kappa}_n, \epsilon)$ and $(\bar{H},\epsilon)$ parameter spaces, which we plot in Fig. S5A and S5B, respectively, where we combine experimental and numerical results.

In Fig. S5A, we find that the natural curvature of the rod can affect the selected mode of the coiling patterns. As κ_n is increased, the basin of existence of the meandering regime is expanded, whereas the translated coiling regime disappears for $\bar{\kappa}_n \gtrsim 0.17$. Moreover, for sufficiently curved rods ($\bar{\kappa}_n \gtrsim 0.17$) and at high values of the dimensionless excess speed ($\epsilon \gtrsim 0.7$), we obtain patterns that fall outside our 4-modes classification scheme (an example of which is given in Fig. S5C). A more thorough analysis of these patterns is beyond the scope of this study. In the limit of $\epsilon \to 1$, however, we do recover the static coiling scenario that was characterized and quantified in the main text.

In the $(\bar{H},\epsilon)$ phase diagram presented in Fig. S5B (obtained for a naturally straight rod) we find that the phase boundaries are approximately perpendicular to the x-axis, which demonstrates that the deployment height, $\bar{H}$, has no significant impact on the selection of the pattern. This result is rationalized below where we find that the various length scales of the meandering patterns vary logarithmically on $\bar{H}$.

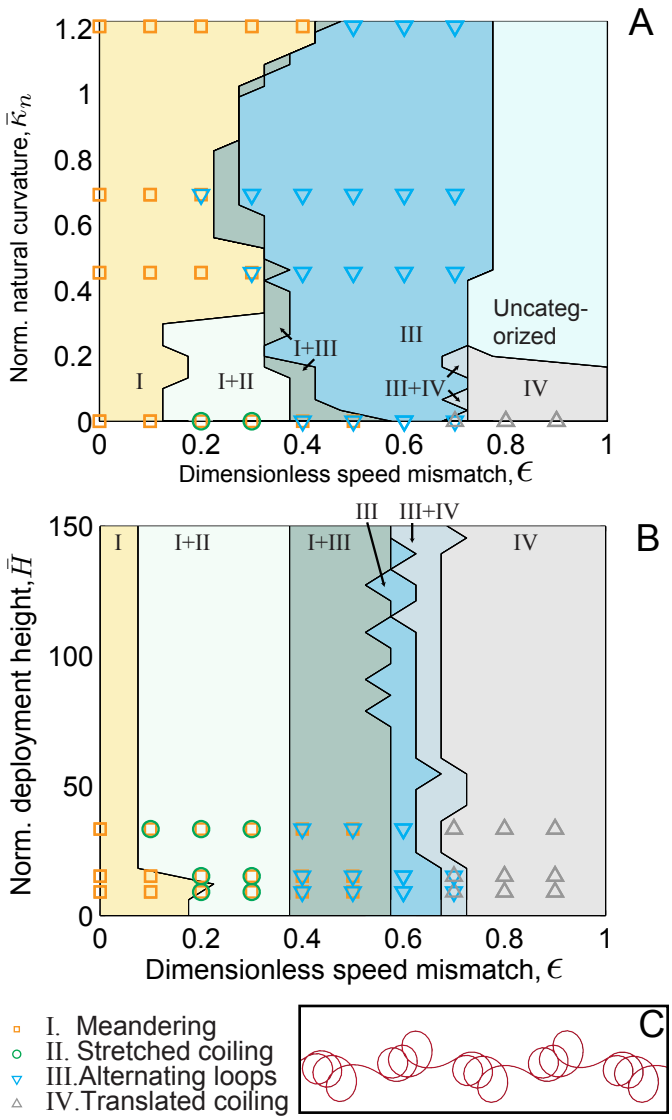

Figure S5: Phase diagrams. The rods used to construct the phase diagrams had a gravito-bending length, $L_{gb} = 3.3$ cm, and deployment height, $\bar{H} = 15$. The physical properties are listed in detail in *Materials and Methods*. (A) Phase diagram of possible patterns in the natural curvature and dimensionless speed mismatch parameter space. (B) Phase diagram of possible patterns in the deployment height and dimensionless speed mismatch parameter space. (C) Simulation image of an uncategorized pattern observed when natural curvature, $\bar{\kappa}_n = 1.0$, and dimensionless speed mismatch, $\epsilon = 0.8$.

S4 Effect of the height of deployment

Having found that the height of deployment has a negligible effect on the coiling patterns (Fig. S5*B*), we now focus on the meandering regime and seek to determine the dependence on $\bar{H}$ of the dimensionless onset wavelength of the pattern, $\bar{\lambda}_0$, (or equivalently, $\bar{A}_0$), from which all other length scales can be determined

using Eq. S2. The final goal is to derive Eq. 6 of the main text, reproduced here again for convenience

$$\bar{\lambda} = \frac{1}{C_2}\left(D_1 \log \bar{H} + \beta\right)(C_1\epsilon + C_2), \tag{S16}$$

where $\bar{\lambda}$ is the dimensionless meandering wavelength, ϵ is the dimensionless speed mismatch, L_{gb} is the gravito-bending length of the rod, C_1 and C_2 are numerical constants that were determined above in § S2, and D_1 and β are new numerical constants that need to be determined.

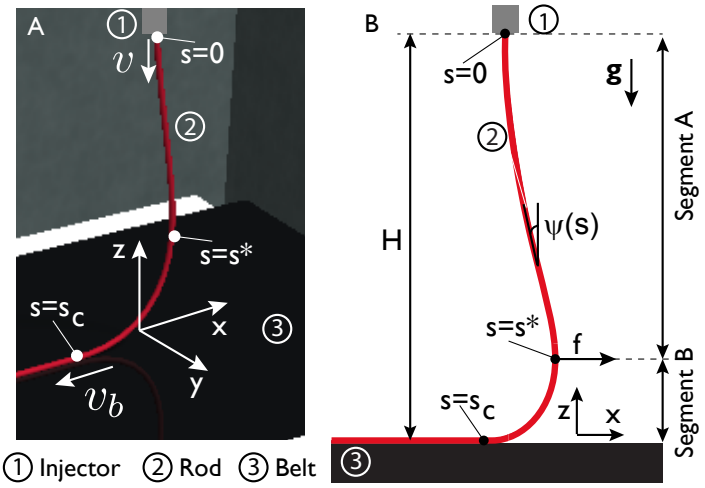

Figure S6: Suspended heel of the rod (red) under gravity, in the weakly nonlinear shape considered for the analysis. (A) Three-dimensional view of the setup. The rod (2) is deployed form the injector (1), onto the rigid belt substrate (3). The injection nozzle is located at $s = 0$ and the contact point between the rod and the belt is at $s = s_c$. The point $s = s^*$ is the location of maximum deflection of the rod. (B) Schematic diagram of the projection into the $x - z$ plane.

In Fig. S6, we present a schematic diagram of the geometry of our setup: Fig. S6*A* is a three-dimensional perspective and Fig. S6*B* is a schematic of the projection onto the $x - z$ plane (x is the direction of motion of the belt.). The rod (in red), has radius r_0, bending stiffness EI, density, ρ, and area of cross section, a, and is deployed from the injector onto the rigid belt substrate (in black). Note that the total arc length of the rod between the injection nozzle (at $s = 0$) and the point of contact with the substrate ($s = s_c$) is slightly larger than H, such that the rod assumes a weakly nonlinear shape. We assume the injector is sufficiently high, *i.e.* $\bar{H} \gg 1$; this assumption is necessary for the analysis below. The point of maximum deflection, located at $s = s^*$, separates the rod into two segments – Segment A for $0 < s < s^*$ and Segment B for $0 < s < s_c$. These two segments exert an equal and opposite force, with horizontal (in the x direction) component f, on each other.

The horizontal coordinate, x, has origin at the injection nozzle, and the vertical one, z, originates at the substrate. The rod, which is assumed to be inextensible, deforms in the $x-z$ plane and its shape can be fully described by the local orientation parameterized by the angle, $\psi(s)$, that its tangent makes with the vertical. The vertical and horizontal tangents are represented by $\psi = 0$ and $\psi = \pi/2$, respectively. Therefore, the boundary condition at the injection point is $\psi(0) = 0$.

Focusing on Segment A of the rod, its total energy can be written as,

$$\mathcal{E}_A = fx(s^*) + \int_0^{s^*} \rho g a z(s) \mathrm{d}s, \tag{S17}$$

where the first term corresponds to the external work done by the horizontal force, f, and the second term is the contribution to the potential energy due to the weight of the rod. Note that in Eq. S17, we have neglected the contribution due to bending given that the bending energy is proportional to the square of the local curvature, $(\mathrm{d}\psi/\mathrm{d}s)^2$, which is assumed to be small along Segment A. This follows from the large deposition height assumption above. Using the geometric relation, $x(s^*) = \int_0^{s^*} \sin\psi \mathrm{d}s$, and the approximation for the vertical coordinates of the rod, $z(s) \sim (s_c - s)\cos\psi(s)$, we can rewrite Eq. S17 as,

$$\mathcal{E}_A \sim f\int_0^{s^*} \sin\psi \mathrm{d}s + \int_0^{s^*} \rho g a(s_c - s)\cos\psi \mathrm{d}s. \tag{S18}$$

We now follow a variational approach and search for equilibrium by minimizing the total energy in Eq. S18. The variation of $\mathcal{E}_A$ due to a small arbitrary perturbation $\delta\psi(s)$ to $\psi(s)$ is,

$$\delta\mathcal{E}_A \sim f\int_0^{s^*} \cos\psi \mathrm{d}s\delta\psi(s) + \int_0^{s^*} \rho g a(s - s_c)\sin\psi \mathrm{d}s\delta\psi(s), \tag{S19}$$

which under the approximation of small angles, $\psi \ll 1$, can be further simplified to,

$$\delta\mathcal{E}_A \sim f\int_0^{s^*} \mathrm{d}s\delta\psi(s) + \int_0^{s^*} \rho g a(s - s_c)\psi \mathrm{d}s\delta\psi(s). \tag{S20}$$

Setting $\delta\mathcal{E}_A = 0$ for an arbitrary perturbation, $\delta\psi(s)$, yields the following expression for the equilibrium shape,

$$\psi(s) \sim \frac{f}{\rho g a(s^* - s)}. \tag{S21}$$

Under the approximation that the arc length of the rod in Segment A is approximately equal to the deployment height, $s^* \sim H$, the x-coordinate of the maximum point of deflection will then scale as,

$$x(s^*) = \int_0^{s^*} \psi(s)ds \sim \frac{f}{\rho g a}\log\left(\frac{H}{D_2 L_{gb}}\right), \tag{S22}$$

where we have introduced the integration constant, $D_2 L_{gb}$, with units of length recalling that gravito-bending length, L_{gb} (defined in Eq. 2 of the main text) is the relevant length scale.

Taking L_{gb} as the characteristic length scale of the system, we can estimate the order of magnitude of the force at $s = s^*$ as $f \sim EI/L_{gb}^2$. Eliminating f from Eq. S22 then gives an expression for $x(s^*)$ in terms of the physical properties of the rod,

$$x(s^*) \sim \frac{EI/L_{gb}^2}{\rho g a}\log\left(\frac{H}{D_2 L_{gb}}\right) \sim L_{gb}\log\left(\frac{H}{D_2 L_{gb}}\right). \tag{S23}$$

We now consider a slightly out-of-plane deformation (with respect to the $x - z$ plane) of the rod to make a meandering pattern onto the belt with very small amplitude, A, and a finite wavelength, λ_0, consistent with the scenario when the dimensionless speed mismatch, ϵ, approaches 0. At the instance when the contact point, s_c, between the rod and the belt is at a peak of a sinusoidal pattern described by

$$y(x) = A\cos\left(\frac{2\pi}{\lambda_0}\left(x(s) - x(s_c)\right)\right), \tag{S24}$$

the curvature at contact, $\kappa\left(x(s_c)\right)$, is

$$\kappa(x(s_c)) = \left|\frac{\mathrm{d}^2 y}{\mathrm{d}x^2}(x(s_c))\right| = \frac{4\pi^2 A}{\lambda_0^2}. \tag{S25}$$

Approximating Segment B as a circular arc with radius $x(s^*)$, the curvature at contact, $\kappa\left(x(s_c)\right)$, is

$$\kappa\left(x(s_c)\right) \sim \frac{1}{x(s^*)} \sim \frac{1}{L_{gb}\log\left(\dfrac{H}{D_2 L_{gb}}\right)}. \tag{S26}$$

Comparing the two expressions for $\kappa\left(x(s_c)\right)$ in Eqns. S25 and S26 yields

$$\frac{A}{\lambda_0^2} \sim \frac{1}{L_{gb}\log\left(\dfrac{H}{D_2 L_{gb}}\right)}. \tag{S27}$$

The geometry of the meandering pattern dictates that the ratio between amplitude and wavelength, in this case A/λ_0, depends only on the dimensionless speed mismatch, ϵ, as derived in Eq. S10. This further simplifies Eq. S27 to provide a scaling law for the onset wavelength, λ_0,

$$\frac{1}{\lambda_0} \sim \frac{1}{L_{gb}\log\left(\dfrac{H}{D_2 L_{gb}}\right)}, \tag{S28}$$

and gives us a closed form expression in terms of the two relevant length scales, L_{gb} and H,

$$\lambda_0 = D_1 L_{gb}\log\left(\frac{H}{D_2 L_{gb}}\right), \tag{S29}$$

where we have introduced the prefactor, D_1, that can not be calculated directly form our scaling analysis but that we have determined through fitting to the DER data in the main text. Eq. S29 can be rewritten in dimensionless form as

$$\bar{\lambda}_0 = D_1 \log\left(\bar{H}\right) + \beta, \tag{S30}$$

where $\bar{\lambda}_0 = \lambda_0/L_{gb}$ and $\bar{H} = H/L_{gb}$ are normalized onset wavelength and deployment height, respectively, and $\beta = -D_1\log\left(D_2\right)$. We can interpret the newly introduced numerical constant β, evaluated through fitting to data, as the dimensionless onset wavelength obtained when the deployment height is equal to the gravito-bending length.

Finally, making use of Eq. S15, we arrive at Eq. S16 that we set out to derive. In the process, we can also identify the characteristic amplitude of the patterns as $\bar{A}_0 = (D_1\log\bar{H} + \beta)/C_2$. This prediction of a logarithmic dependence of the onset wavelength on deployment height is indeed observed in the DER simulations, as confirmed by the data in the inset of Fig. 4F of the main text.

Role of twist. In the derivation of the closed-form solution for the wavelength in Eq. S30, we assumed that there is a balance between bending and gravitational energy in Segment B of the rod and that twist energy is negligible (along with inertia). We have turned to the DER simulations to assess the validity of this assumption and performed a quantitative comparison between gravitational, bending, and twisting energies. As such, we evaluate the various energetic contributions, integrated over the total arclength of Segment B, to get the bending energy $E_b = \int_{s^*}^{s_c} \mathcal{E}_b \mathrm{d}s$, twisting energy $E_t = \int_{s^*}^{s_c} \mathcal{E}_t \mathrm{d}s$, and gravitational energy $E_g = \int_{s^*}^{s_c} \mathcal{E}_g \mathrm{d}s$, where $\mathcal{E}_b, \mathcal{E}_t$, and $\mathcal{E}_g$ denote the corresponding energies *per unit length*, as defined in the main manuscript.

In Fig. S7, we plot the times-series of the energy ratios for meandering mode, and find the bending and gravitational energies to be of the same order of magnitude ($E_b/E_g \sim 1$), whereas the twisting energies are negligible compared to both bending and gravity as evident from the plot $E_t/E_b \ll 1, E_t/E_g \ll 1$; both of these ratios are at most 10^{-3}.

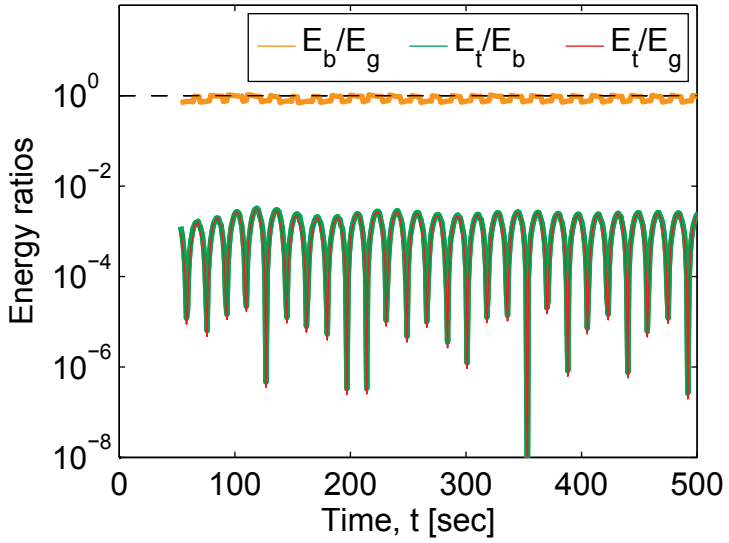

Figure S7: The comparison between twisting E_t and bending E_b in the segment B and the gravitational potential E_g below the maximal deflection, for meandering at $\epsilon = 0.9$. The relative levels of different energies are illustrated by the pairwise ratios E_b/E_g, E_t/E_b and E_t/E_b. A rod with $L_{gb} = 3.3$ cm was deployed from $\bar{H} = 15$cm in DER simulations.

S5 Approximate value of onset wavelength

In the previous section we analyzed the non-dimensionalized onset wavelength $\bar{\lambda}_0$ and derived Eq. S30 which contains fitting parameters (prefactors) D_1 and β that cannot be calculated theoretically. However, over the range of $\bar{H}$ values used in most of our experiments (H between 50cm and 110cm), the variation of $\log \bar{H}$ is relatively small (between 2.7 and 3.5) and can be approximated as a constant. This simplification means that, if we ignore the change of onset wavelength due to H, then $\bar{\lambda}_0$ can be treated a constant, or in other words, the onset wavelength λ_0 is proportional to the gravito-bending length scale L_{gb}. In this section we attempt to predict this constant value by considering the torque that the suspended heel exerts on the contact point when it is at a peak of the sinusoidal pattern. Fig. S8 shows the configuration of such an instance of time. Recall that the sinusoidal pattern is described by

$$y(x) = A \cos \frac{2\pi x}{\lambda}. \tag{S31}$$

The rod between $s = s^*$ and $s = s_c$ (*i.e.* Segment B from the last section) is pulled away from the vertical position and tilted towards the y direction, because the contact point is at its maximal displacement, $y(0) = A$. This slanted configuration increases the gravitational potential of the rod segment, creating a restoring force f, analogous to a pendulum. However, given the circular shape of the segment (refer to Fig. S6), this force does not act directly on the contact point. In the belt's plane, the rod segment can be approximated by an *imaginary* beam that is tangentially connected to the rod at the contact point (the red line in Fig. S8), on whose opposite end the restoring force acts (the green arrow for f in Fig. S8). Assuming that the segment has radius L_{gb}, the length of the beam is thus L_{gb}. Therefore, the moment at the contact point due to this force is $M = -fL_{gb}$. Force balance at the contact point requires that the bending moment $EI\kappa$ in the rod is equal to M, where κ is the curvature at the contact point. In the limit of small ϵ (and thus small A), κ can be approximated by $y''(0)$, yielding

$$EIy''(0) = -fL_{gb}. \tag{S32}$$

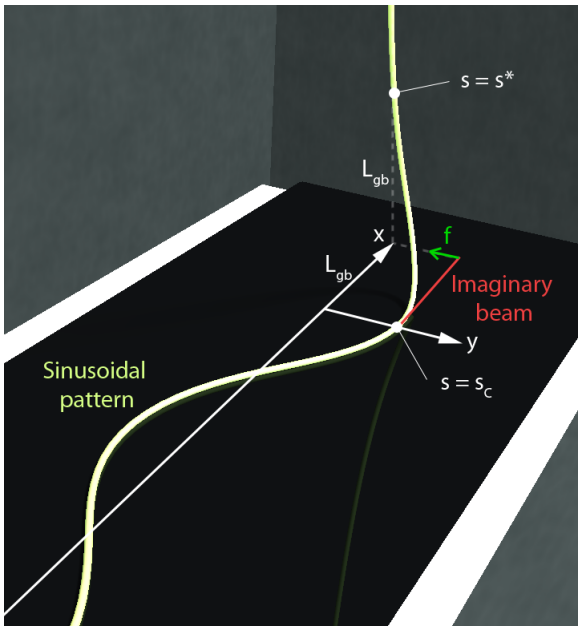

Figure S8: The configuration when the contact point is at a peak of the sinusoidal pattern. Segment B (between $s = s^*$ and $s = s_c$) is displaced in the y direction like a pendulum.

According to Eq. S31, $y''(0) = -\dfrac{4\pi^2 A}{\lambda^2}$. Thus

$$\frac{4\pi^2 EIA}{\lambda^2} = fL_{gb} \tag{S33}$$

On the other hand, the horizontal restoring force f can be estimated by approximating segment B with a pendulum of vertical length L_{gb}:

$$f = \frac{\rho g \pi r_0^2}{2} y(0) = \frac{\rho g \pi r_0^2 A}{2}. \tag{S34}$$

Combining this with Eq. S33, we obtain

$$8\pi^2 EI = \rho g \pi r_0^2 L_{gb} \lambda^2, \tag{S35}$$

$$\lambda = \sqrt{\frac{8\pi EI}{\rho g r_0^2 L_{gb}}} = \sqrt{\frac{2\pi^2 r_0^2 E}{\rho g L_{gb}}} = \sqrt{16\pi^2 L_{gb}^2} = 4\pi L_{gb}, \tag{S36}$$

$$\bar{\lambda} = 4\pi. \tag{S37}$$

Since the analysis above assumes infinitesimal ϵ, the wavelength obtained here is in fact the onset wavelength $\bar{\lambda}_0$. The value of the prefactor, 4π, agrees roughly with the values of D_1 and β from data fitting: substituting $D_1 = 1.27$, $\beta = 7.00$ and $\bar{H} = 15.2$ into Eq. S30 yields $\bar{\lambda}_0 = 10.5$.

S6 Effect of natural curvature

In the manuscript, we found the normalized onset wavelength, $\bar{\lambda}_0$, for a naturally curved rod to be well described by

$$\bar{\lambda}_0(\bar{\kappa}) = \begin{cases} \bar{\lambda}_0(0), & \text{for } \bar{\kappa} < \bar{\kappa}_c \\ -\bar{B}_1^2 \bar{\kappa}_n + \bar{B}_2, & \text{for } \bar{\kappa}_n > \bar{\kappa}_c, \end{cases} \tag{S38}$$

where $\bar{\kappa}_c$ is the normalized critical curvature, and $\bar{B}_1$, and $\bar{B}_2$ are two numerical constants. In Fig. 5C of the manuscript, we plotted $\{\bar{B}_1, \bar{B}_2, \bar{\kappa}_c\}$ as functions of the gravito-bending length, L_{gb}, at a fixed deployment height $\bar{H} = 15$, and found these parameters to stay constant with L_{gb}. To demonstrate that this finding holds, regardless of $\bar{H}$, in Fig. S9(A-B) we plot $\{\bar{B}_1, \bar{B}_2, \bar{\kappa}_c\}$ against L_{gb} at two higher deployment heights $\bar{H} = \{61, 121\}$, again finding no variation with L_{gb}. The values of the parameters fitted in Fig. S9 for $\bar{H} = \{61, 121\}$ are $\bar{B}_1 = \{2.04 \pm 0.01, 2.21 \pm 0.02\}$, $\bar{B}_2 = \{12.7 \pm 0.02, 13.6 \pm 0.10\}$, and $\bar{\kappa}_c = \{0.126 \pm 0.004, 0.118 \pm 0.005\}$.

In Fig. S9(C-D), we plot $\bar{B}_1$, and $\bar{B}_2$ as a function of $\bar{H}$ at a fixed gravito-bending length $L_{gb} = 3.3$ cm. Using Eq. 8 of the manuscript, this is used to calculate the critical natural curvature, $\bar{\kappa}_c$, plotted in Fig. 5*D* of the main text as a function of $\bar{H}$. There is a logarithmic dependence of $\bar{B}_1$, and $\bar{B}_2$ on deployment height, $\bar{H}$, especially at high $\bar{H}$; its detailed understanding is beyond the scope of this study.

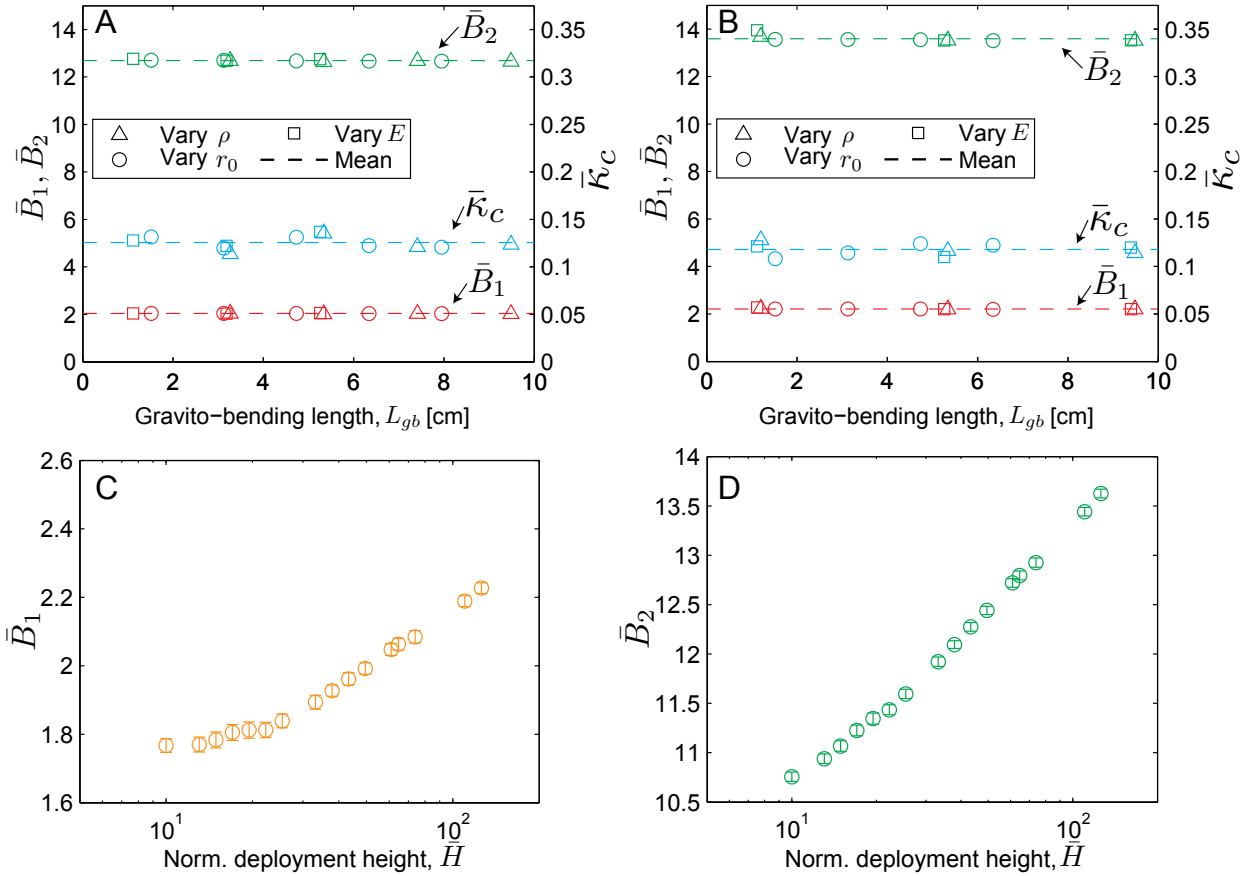

Figure S9: Normalized critical curvature, $\bar{\kappa}_c$, along with the parameters $\bar{B}_1, \bar{B}_2$ used to calculate it (Eq. 8 in the manuscript), as a function of the gravito-bending length, L_{gb}, at the fixed deployment heights of (A) $\bar{H} = 61$, and (B) $\bar{H} = 121$. To vary L_{gb}, we followed a similar procedure to that used to produce Fig. 4*F* in the manuscript. (C) $\bar{B}_1$ as a function of $\bar{H}$ at $L_{gb} = 3.3$ cm. (D) $\bar{B}_2$ as a function of $\bar{H}$ at the same L_{gb}.

S7 Numerical simulations

S7.1 Method

We used a numerical tool based on DER to perform simulations, side by side with the experiments. The method derives discrete versions of the equations of motion from scratch, instead of discretizing smooth

equations, thus capturing important aspects of the underlying physics, which are often lost in the discretization process. Our code represents the rod by its centerline along with a material frame. The material frame is itself represented as the angular deviation from a reference frame, which is maintained across time steps using parallel transport. Stretching and bending are naturally captured by the deformation of the centerline, while twisting about the center line is described by the rotation of the material frame.

The contact model is briefly introduced in the Materials and Methods section of the main text. For clarity we describe our implementation of the boundary condition in more details below.

Classification. Simulation nodes and edges (jointly "degrees of freedom") are classified as either *constrained* (under the direct influence of boundary conditions) or *free* (under the influence of the equations of motion for the dynamics of a Kirchhoff elastic rod, absent of boundary conditions). In the following, we describe the modifications required to integrate the dynamics of constrained degrees of freedom, and to transition between the two states.

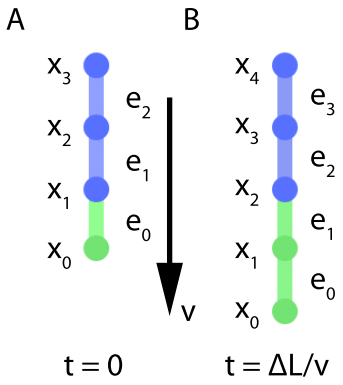

Figure S10: The injector boundary condition. (A) The beginning of the simulation. (B) After injecting ΔL of rod. Blue nodes and edges are constrained; green nodes and edges are free.

Injector Boundary Condition. At any point during the simulation, three nodes and two edges are constrained to model the boundary condition of the rod near the injector. Consider the initial conditions, in which constrained nodes x_1 through x_3 and edges e_1 through e_2 constitute the *injector boundary conditions* (Fig. S10 A). Under these conditions, each nodal position is prescribed to move downward with fixed downward velocity v; each edge material frame is prescribed to remain fixed, such that the natural curvature is aligned to the belt velocity, $\mathbf{v}_b$.

After a duration $\frac{\Delta L}{v}$ elapses (Fig. S10 B), we lift the constraints on node x_1 and edge e_1, allowing them to simulate as free degrees of freedom under the equations of motion. Simultaneously, we introduce the new constrained edge e_3 and vertex x_4, corresponding to the injection of additional rod. The lifting of constraints on x_1 and e_1, combined with the introduction of constrained degrees of freedom e_3 and x_4, maintain the invariant that four nodes are constrained to model the injector boundary condition.

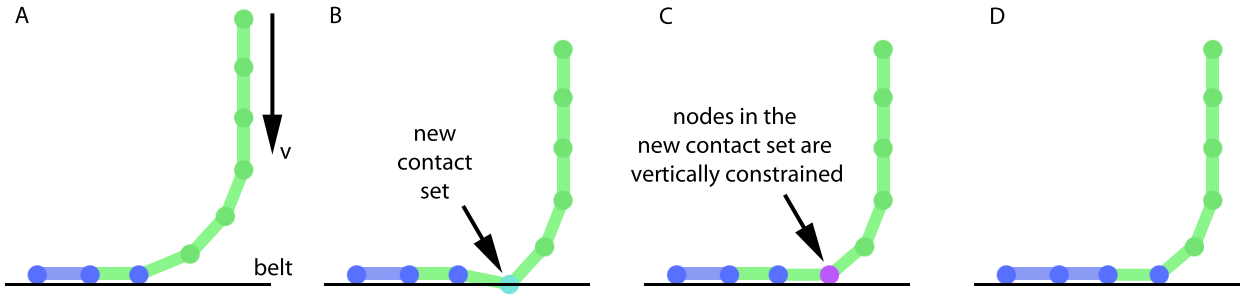

Figure S11: The belt boundary condition. (A) Beginning of the time step. (B) The predictor step, where the new contact set is detected. (C) The corrector step, where the nodes in the new contact set are vertically constrained. (D) The vertically constrained nodes become fully constrained as its horizontal velocity becomes small.

Belt Contact Boundary Condition. Once the free end of the rod contacts the belt (the plane of $z = 0$), a new constraint must be introduced to model the contact. We must first detect the contact, and then respond. Correspondingly, each simulation step begins with a *predictor* step, optionally followed by a *corrector* step.

The *predictor* step is performed by ignoring the direct effect of the belt on free degrees of freedom. At the end of the predictor step, we determine whether any free nodes have made contact with belt (see Fig. S11 B). Such nodes form the *new contact set*, Ξ. Contact is defined as $z_i \leq z_{belt} + r_0$ where z_i is the z coordinate of the node, z_{belt} is the z coordinate of the belt, and r_0 is the rod radius.

If new contacts have been identified, a *corrector* step is required (Fig. S11 C). We rewind the simulation to the start of the time step. The vertical coordinate z of each node in the new contact set, Ξ, is transitioned from the free state to the constrained state, with vertical position prescribed to lie in contact with the belt, i.e., $z = z_{belt} + r_0$. For these *vertically-constrained* nodes, the horizontal coordinate degrees of freedom (x, y) continue to be governed by the equations of motion. After introducing the vertical constraints, we integrate forward in time again, now assured that the nodes previously in the new contact set cannot penetrate through the belt. At the end of the corrector step, each vertically-constrained node is transitioned either to the free or the (fully) constrained state: if the relative velocity between the node and the belt is below a threshold (we use 10^{-6} cm/s), we permanently constrain the node to follow the belt, i.e., to maintain the belt velocity (Fig. S11 D). Otherwise, we free the node. Because we focus on the small Froude number regime, where inertial effects are negligible, we observe that, typically, vertically-constrained nodes are fully belt-constrained after the corrector step.

The first of the constrained node, counting from the suspended heel, is called the contact point node. As explained in the main text, all the edges that are more than αL_{gb} away from the contact point vertex into the fixed portion are prevented from rotating by a constraint on the material frame angle.

S7.2 Source code

The source code of our numerical simulation tools has been made available at `http://www.cs.columbia.edu/cg/elastic_coiling/`. Instructions on how to use the program are also provided on the webpage.